

Full tensorial characterization of PZN-12PT single crystal by Resonant Ultrasound Spectroscopy

T. Delaunay^a, E. Le Clézio^a, M. Guennou^b,

H. Dammak^b, M. Pham Thi^c, G. Feuillard^a

^a Université François Rabelais de Tours,

Laboratoire UltraSons Signaux et Instrumentation, FRE 2448 CNRS,

ENIVL Rue de la Chocolaterie, BP3410,

41034 BLOIS CEDEX, FRANCE

^b Laboratoire SPMS, UMR 8580 CNRS,

Ecole Centrale Paris, F-92295 Châtenay-Malabry, France

^c Thales Research & Technology France,

F-91767 Palaiseau, France

Abstract

An experimental set-up, based on the electrical excitation of a piezoelectric sample, is proposed for resonant ultrasound spectroscopy measurements. The detection of the mechanical vibrations is performed by means of a laser interferometer. In par-

allel, the free vibrations of piezoelectric parallelepipeds of tetragonal and hexagonal symmetries are modeled, taking into account the effect of the sample metalization. Finally, the paper presents the full elastic, piezoelectric and dielectric tensors of two PMN-34.5%PT ceramic and PZN-12%PT single crystal cubes.

1 Introduction

Relaxor-based ferroelectric single crystals such as PMN-x%PT and PZN-x%PT can have excellent piezoelectric properties compared to conventional PZT ceramics. Their large electromechanical coefficient k_{33} (about 93%), their high dielectric permittivity ε_{33}^T (about $5000\varepsilon_0$) and their typical piezoelectric constant d_{33} of 2500pC/N make these materials very attractive for ultrasonic transducer applications requiring a high sensitivity and large bandwidths [1, 2] or for sensors and actuators.

Nowadays, to design complex devices, manufacturers need to have the complete sets of properties of the constitutive materials. As a consequence, the existing characterization methods have to be adapted to the small dimensions of single crystals, their anisotropy degree and the difficulty to obtain homogeneous compositions [3, 4, 5]. Complete tensor properties has already been reported for PMN-x%PT and PZN-x%PT single crystals. However, both electrical and acoustic measurements were performed involving the preparation of at least five samples [6, 7] leading to possible differences in the sample characteristics. Another method, based on the transmission of acoustic waves through immersed plates, has been successfully applied to the characterization of large samples [8, 9]. However, this method cannot be easily adapted to single crystals due to the re-

quired dimensions of the tested samples.

The method reported in this paper is based on the Resonant Ultrasound Spectroscopy (RUS) allowing to identify the complete set of elastic, piezoelectric and dielectric properties of materials with only one single small sample. This method was first successfully applied to elastic materials [10, 11, 12] and then extended piezoelectric samples [13, 14]. But in these later cases, mechanical excitations and detections were performed, involving transducers or pinducers limiting the frequency bandwidth. Moreover, the free boundary conditions were not necessarily satisfied and all the excited modes were not electrically coupled. Furthermore these methods were only developed for materials with trigonal symmetry.

In this paper, a new experimental set-up is proposed for resonant ultrasound spectroscopy measurements. It is based on an electrical excitation of the piezoelectric sample and on the detection of its mechanical vibrations by means of a laser interferometer. In parallel, the free vibrations of piezoelectric parallelepipeds of tetragonal and hexagonal symmetries have been modeled. The effect of the sample metalization is discussed and results are compared to finite element computations. To validate the experimental set-up and the inverse problem resolution, a $10 \times 10 \times 10 \text{ mm}^3$ cube of PMN-34.5%PT ceramic (hexagonal symmetry $6mm$) with known properties is first characterized. Then, the paper reports for the first time the entire set of properties of a $[001]_c$ PZN-12%PT single crystal in the tetragonal phase ($4mm$).

2 Modeling of the resonant vibration modes of piezoelectric parallelepipeds

2.1 Free vibrations of a piezoelectric parallelepiped

Consider a non metalized parallelepiped with characteristic dimensions $L_1 = \frac{A}{2}$, $L_2 = \frac{B}{2}$, $L_3 = \frac{C}{2}$ as shown in Figure 1. The axis are positioned so that they cut the orthogonal face in its center. The Lagrangian of a piezoelectric body is [15, 16, 13]:

$$L = \frac{1}{2} \iiint_v u_{i,j} C_{ijkl}^E u_{k,l} + 2\phi_{,m} e_{mkl} u_{k,l} dV - \frac{1}{2} \iiint_v \phi_{,m} \varepsilon_{mn}^S \phi_{,n} + \rho \omega^2 u_i u_i dV, \quad (1)$$

where a $e^{i\omega t}$ time dependence is assumed for mechanical and electrical quantities. In a variational approach, any mechanical displacement, $u_i \rightarrow u_i + \delta u_i$, and electrical potential variation, $\phi \rightarrow \phi + \delta \phi$, yield a variation of the Lagrangian: $L \rightarrow L + \delta L$. Hamilton's principle leads to look for the Lagrangian stationary points where $\delta L = 0$. This determines a motion equation whose solutions correspond to the free vibrations of the piezoelectric body. In the Rayleigh-Ritz method [16], the mechanical displacements and the electrical potential are expressed as a linear combination of functions:

$$\mathbf{u} = \sum_{p=1}^N a_p \boldsymbol{\psi}_p \quad ; \quad \phi = \sum_{r=1}^M b_r \varphi_r. \quad (2)$$

The $\boldsymbol{\psi}_p$, $p = 1, \dots, N$, and φ_r , $r = 1, \dots, M$, functions are chosen to be orthonormal.

To solve the variational problem a_p and b_r constants have to be determined. Substituting

expressions (2) into equation (1), the Lagrangian becomes:

$$L = \frac{1}{2} \left[\sum_p \sum_{p'} a_p a_{p'} (\Gamma_{pp'} - \rho \omega^2 \delta_{pp'}) \right] + \frac{1}{2} \left[2 \sum_p \sum_r a_p b_r \Omega_{pr} - \sum_r \sum_{r'} b_r b_{r'} \Lambda_{rr'} \right], \quad (3)$$

where,

$$\begin{aligned} \Gamma_{pp'} &= \iiint_v \psi_{pi,j} C_{ijkl}^E \psi_{p'k,l} dV, \\ \Omega_{pr} &= \iiint_v \varphi_{r,m} e_{mkl} \psi_{pk,l} dV, \\ \Lambda_{rr'} &= \iiint_v \varphi_{r,m} \varepsilon_{mn}^S \varphi_{r',n} dV, \end{aligned} \quad (4)$$

with

$$\psi_{pi,j} = \frac{1}{2} \left(\frac{\partial \psi_{pi}}{\partial x_j} + \frac{\partial \psi_{pj}}{\partial x_i} \right) \text{ and } \varphi_{r,m} = \frac{\partial \varphi_r}{\partial x_m}. \quad (5)$$

ψ_{pi} is the $\psi_{\mathbf{p}}$ component in the \mathbf{x}_i direction. $\mathbf{\Gamma}$, $\mathbf{\Omega}$ et $\mathbf{\Lambda}$ are respectively called elastic, piezoelectric and dielectric interaction matrices [15]. Coefficients a_p and b_r are then determined by the condition of the stationary Lagrangian:

$$\frac{\partial L}{\partial a_p} = 0, \quad p=1,2,3,\dots,N; \quad \frac{\partial L}{\partial b_r} = 0, \quad r=1,2,3,\dots,M. \quad (6)$$

From equations (4) and (6), the eigenvalue problem is expressed as:

$$(\mathbf{\Gamma} + \mathbf{\Omega} \mathbf{\Lambda}^{-1} \mathbf{\Omega}^t) \mathbf{a} = \rho \omega^2 \mathbf{a}, \quad (7)$$

$$\mathbf{b} = \mathbf{\Lambda}^{-1} \mathbf{\Omega}^t \mathbf{a}, \quad (8)$$

where $\mathbf{a} = (a_1, a_2, \dots, a_N)^t$ and $\mathbf{b} = (b_1, b_2, \dots, b_M)^t$ are unknown vectors. A description of the matrices $\mathbf{\Gamma}$, $\mathbf{\Lambda}$ et $\mathbf{\Omega}$ is given in the appendix of [13]. The determination of the

eigenvalues $\rho\omega^2$ and the eigenvectors \mathbf{a} and \mathbf{b} allows then to identify the resonant frequency ω , the modal elastic displacements \mathbf{u} and the electric potential ϕ , respectively.

As pointed in literature [17], a Legendre polynomial basis is very well adapted to describe the behavior of the electrical and acoustical fields inside parallelepipeds. As a consequence, the solutions of the eigenproblem (7) and (8) are sought in the form [13, 18]:

$$\boldsymbol{\psi}_{\mathbf{p}} = \frac{1}{\sqrt{L_1 L_2 L_3}} \bar{P}_\lambda\left(\frac{x_1}{L_1}\right) \bar{P}_\mu\left(\frac{x_2}{L_2}\right) \bar{P}_\nu\left(\frac{x_3}{L_3}\right) \mathbf{e}_{\mathbf{i}}, \quad (9)$$

$$\varphi_r = \frac{1}{\sqrt{L_1 L_2 L_3}} \bar{P}_\xi\left(\frac{x_1}{L_1}\right) \bar{P}_\varsigma\left(\frac{x_2}{L_2}\right) \bar{P}_\eta\left(\frac{x_3}{L_3}\right), \quad (10)$$

where the p^{th} and r^{th} basic functions $\boldsymbol{\psi}_{\mathbf{p}}$ and φ_r are defined by the triplets (λ, μ, ν) and (ξ, ς, η) , respectively. $\bar{P}_\alpha(x)$ is the Legendre function of order α and $\mathbf{e}_{\mathbf{i}}$ is the unit displacement vector in the direction $\mathbf{x}_{\mathbf{i}}$. $\frac{1}{\sqrt{L_1 L_2 L_3}}$ is a normalization term.

2.2 Symmetry considerations

Mochizuki showed that the symmetry classification of the free oscillations of anisotropic parallelepipeds was useful for material characterization [19]. It allows to discretize the matrices of the eigenvalue problem (7) and then to simplify its resolution. This principle is here extended to piezoelectric materials of parallelepiped shapes. The samples characterized in the present study belong, at least, to the mmm symmetric class, direct product of the 222 class and the inversion $\bar{1}$:

$$mmm = 222 \otimes \bar{1}. \quad (11)$$

The free modes of vibration of a parallelepiped can then be classified according to the eight following elements [19], expressed here in their irreducible representation (Mulliken

notation [20]):

$$A_g, B_{1g}, B_{2g}, B_{3g}, A_u, B_{1u}, B_{2u}, B_{3u}. \quad (12)$$

The elastic displacements and the electric potential - equations (2), (9) and (10) - are then:

$$\mathbf{u} = \sum_{\lambda\mu\nu i} \frac{a_{\lambda\mu\nu i}}{\sqrt{L_1 L_2 L_3}} \bar{P}_\lambda \left(\frac{x_1}{L_1} \right) \bar{P}_\mu \left(\frac{x_2}{L_2} \right) \bar{P}_\nu \left(\frac{x_3}{L_3} \right) \mathbf{e}_i, \quad (13)$$

$$\phi = \sum_{\xi\varsigma\eta} \frac{b_{\xi\varsigma\eta}}{\sqrt{L_1 L_2 L_3}} \bar{P}_\xi \left(\frac{x_1}{L_1} \right) \bar{P}_\varsigma \left(\frac{x_2}{L_2} \right) \bar{P}_\eta \left(\frac{x_3}{L_3} \right). \quad (14)$$

The relations between the coefficients $a_{\lambda\mu\nu i}$ and $b_{\xi\varsigma\eta}$ and the symmetry groups are presented in Table 1 which also classifies the eigenmodes with respect to their irreducible representations and the Legendre polynomials' parity [19, 17]. Table 1 is valid for piezoelectric materials possessing at least the orthorhombic symmetry.

Using this decomposition, the interaction matrices $\mathbf{\Gamma}$, $\mathbf{\Omega}$ and $\mathbf{\Lambda}$ are separated into eight independent matrices, leading to eight independent eigenvalue problems:

$$\left\{ \begin{array}{l} (\mathbf{\Gamma}_h + \mathbf{\Omega}_h \mathbf{\Lambda}_h^{-1} \mathbf{\Omega}_h^t) \mathbf{a} = \rho \omega^2 \mathbf{a} , \\ \text{with,} \\ h = A_g, B_{1g}, B_{2g}, B_{3g}, A_u, B_{1u}, B_{2u}, B_{3u}. \end{array} \right. \quad (15)$$

This size reduction of the eigenvalue problems to be solved yields reduced computation times. Table 2 presents the classification of the resonance frequencies and corresponding mode-shapes of a $10 \times 10 \times 10 \text{ mm}^3$ PMN-34.5%PT cube (see §3.1). Due to the fact that the studied samples are cubic ($L_1 = L_2$), two modes are degenerated (B_{2g} , B_{3g} and B_{2u} , B_{3u}) and their mode-shapes are similar with respect to a 90° rotation around the \mathbf{x}_3 axis.

2.3 Modeling of piezoelectric cube eigenmodes in the presence of electrodes

To perform the electric polarization of piezoelectric materials, electrodes have to be laid down on two surfaces, generally orthogonal to the polarization axis. Expression (1) does not take into account any potential imposed by an electrode on the piezoelectric solid surface. To do so, the work performed by the electrical charges of the metalized surfaces has to be subtracted from the Lagrangian (1). Neglecting the mass of the electrodes and considering two metalized surfaces $A_{1,2}$, the Lagrangian becomes:

$$\begin{aligned}
L &= \frac{1}{2} \iiint_v u_{i,j} C_{ijkl}^E u_{k,l} + 2\phi_{,m} e_{mkl} u_{k,l} d\tau \\
&- \frac{1}{2} \iiint_v \phi_{,m} \varepsilon_{mn}^S \phi_{,n} + \rho \omega^2 u_i u_i d\tau \\
&- \sum_{m=1}^2 \iint_{A_m} \phi n_i (e_{ikl} u_{k,l} - \varepsilon_{ij}^S \phi_{,i}) dA_m,
\end{aligned} \tag{16}$$

where the surface integral represents the energy generated by the electrostatic forces $\sigma \mathbf{E}$. In our case - on a metalized surface supposed to be located at $x_3 = -L_3$ - a constant electrical potential is assumed to be zero:

$$\phi(x, y, z) = 0 \quad \forall (x, y, z) \in (x, y, -L_3). \tag{17}$$

The "surface" term of equation (17) vanishes but the above condition influences the choice of the functions describing the electrical potential in equation (2). Trigonometric or polynomial functions can still be used but they must have a high order to allow a numerical convergence. To avoid long computation times, Legendre functions are here weighted by a simple polynomial in order to satisfy the equation (17). The potential functions φ_r ($r = 1, \dots, M$) then become:

$$\varphi_r = \frac{1}{\sqrt{L_1 L_2 L_3}} \bar{P}_\xi \left(\frac{x_1}{L_1} \right) \bar{P}_\varsigma \left(\frac{x_2}{L_2} \right) f_\eta \left(\frac{x_3}{L_3} \right), \quad (18)$$

where

$$f_\eta(x_3) = \left[\frac{(-1)^\eta}{2} (1 + x_3) P_\eta(x_3) \right]. \quad (19)$$

The mechanical displacement formulation is not modified. However, the orthogonality relation - not necessarily required - is no longer verified. The definitions of the matrices Γ , Λ et Ω - given in the appendix of [13] - can still be used but the constitutive blocks are modified. A description of the resulting modifications is given in the appendix A. These matrices allow to solve the eigenvalue problem (7).

3 Theoretical results and discussion

3.1 Application to PMN-34.5%PT and comparison with a finite element modeling

The variational model is here applied to the computation of the resonant frequencies and mode-shapes of a PMN-34.5%PT Manganese doped ceramic cube. Its dimensions are chosen to be $10 \times 10 \times 10 \text{ mm}^3$, to be consistent with the experiments presented in §4. The characteristics of the ceramic are taken from the literature [21] where the symmetry class is supposed to be hexagonal ($6mm$): density $\rho = 8060 \text{ kg}\cdot\text{m}^{-3}$; elastic stiffness coefficients (at constant E) $C_{11}^E = C_{22}^E = 168.8 \text{ GPa}$, $C_{12}^E = 116.83 \text{ GPa}$, $C_{13}^E = C_{23}^E = 116.80 \text{ GPa}$, $C_{33}^E = 154.43 \text{ GPa}$, $C_{44}^E = C_{55}^E = 30.56 \text{ GPa}$, $C_{66}^E = 25.97 \text{ GPa}$; the piezoelectric constants

$e_{15} = e_{24} = 16.66 \text{ pC}\cdot\text{m}^{-2}$, $e_{31} = e_{32} = -6.92 \text{ pC}\cdot\text{m}^{-2}$, $e_{33} = 30.15 \text{ pC}\cdot\text{m}^{-2}$; the dielectric constants (at constant strain) $\varepsilon_{11}^S = \varepsilon_{22}^S = 2367\varepsilon_0$, $\varepsilon_{33}^S = 2622\varepsilon_0$.

A convergence criterion is employed to fix the order n of the Legendre functions used in the decomposition (9) and (10): the difference between the results obtained with the order n and those of the order $n+1$ must be less than 0.1%. In the following computations, n is set to 10. The first six resonances correspond to the six static modes (three rotations and three translations). As a consequence, their resonant frequencies are null. The 24 following resonant frequencies, given by the eigenvalues of the matrix $\mathbf{\Gamma} + \mathbf{\Omega}\mathbf{\Lambda}^{-1}\mathbf{\Omega}^t$, are presented in Table 3. Some of the values presented in Table 3 are redundant. They correspond to the same kind of mode with respect to a 90° rotation around the \mathbf{x}_3 axis. This is a consequence of the material symmetry as well as the chosen geometry ($L_1 = L_2$). Table 3 also reports the resonance frequencies calculated using Atila FEM code. In this case, a cubic mesh with 20 nodes has been chosen and 6 elements have been used to model each side. It lead to 1225 points. It can be seen that the resonances computed by the FE code are generally higher than the ones of the variational method. However, the maximum relative error is of 1.23% allowing to consider that the two sets of results are consistent.

The determination of the a_p components, identified by the matrix eigenvectors, allows to compute the three displacements u_1 , u_2 and u_3 and then reconstruct the vibration mode-shapes corresponding to the resonant frequencies. The electrical potential can be also reconstructed from the b_r components from the relation (8). Figure 2 presents the elastic displacement ((a) and (b)) and the electric potential ((c) and (d)) computed at the upper surface ($x_3 = L_3$) by the variational method ((a) and (c)) and the FE code ((b)

and (d)). The resonant frequencies are respectively 114431 Hz and 114450 Hz. The two sets of results are in good agreement.

3.2 Effect of metalization

In the experiments presented in section 4, one of the electrodes is partially removed to control the localization of the sample excitation. The corresponding face is then supposed to be free of metalization. The effect of the remaining electrode on the resonant behavior of the cube is here studied. The eigenvalue problem is then modified to take into account the effect of one electrode (see §2.3). The results are compared to Finite Element simulations. The same nodes and mesh than for the non metalized case are used in the Atila FE code but the electrical potential is imposed to be null on the face $(x, y, -L_3)$ of the cube. Table 4 presents the comparison between the resonant frequencies obtained by the two models. First of all, it must be noticed that the two sets of results are in good agreement. For the two methods, only specific modes are sensitive to the electrode. The mean influence of the metalization is 1.3 % and the maximum difference with the non metalized case is 4.7 %. No significant modification on the mechanical mode-shapes on the metalized surface has been observed. As a consequence, in the following, the effect of the electrode will be neglected and symmetry considerations will be supposed to be valid. Note that the metalization has already been neglected in experimental studies [14] but, to the authors' knowledge, Table 4 seems to give the first theoretical demonstration of its low influence.

4 Experimental results and discussion

This section presents the experimental set-up developed to generate and detect the free vibration of a piezoelectric cube. Two materials have been tested. First of all, the vibrations of a PMN-34.5%PT ceramic (hexagonal symmetry 6mm) with known properties (see §3.1) are measured to validate the method. Then, the free vibrations of a cube of single crystal in the tetragonal phase 4mm (PZN-12%PT) are monitored in a way to identify its characteristics. Both samples have been manufactured by Thales, Research & Technology (Orsay) and the PZN-12%PT cube has been prepared by the Laboratoire des Structures, Propriétés et Modélisation des Solides (Paris).

4.1 Experimental set-up and materials

Several methods have already been employed to perform acoustic spectroscopy on parallelepipeds. They generally involve pinducers or ultrasonic transducers positioned at the sample corners [18, 22, 14]. These methods are inherently limited by the transducer bandwidths leading to an inhomogeneous mode excitation. To avoid these problems, an electrical excitation is performed in the present study. It is delivered through an impedance analyzer (Agilent 4395A) also allowing to measure the sample electrical resonances and anti-resonances (Figure 3(a)). It has a very large frequency bandwidth (10kHz - 500MHz) and the delivered electrical power is set to 0 dBm to 10 dBm depending on the excited mode. The sample is set on a plastic holder and the electrical contact is ensured by a metallic strip fixed on a spring so that the free mechanical boundary conditions at the surfaces of the cube are fulfilled.

Velocity measurements at the surface of the sample are performed by means of a Laser vibrometer (Polytech OFV-505) in a way to detect resonance frequencies and the associated mode-shapes. The interferometer is positioned at 50 cm from the sample leading to a 20 μm focal area. The velocity decoder sensitivity is respectively 5 mm/s/V and 25 mm/s/V, depending on the cut-off frequency, respectively 250 kHz and 1,5 MHz. The measured signals are sent to a computer via an oscilloscope (LeCroy 6050A) that performs a FFT with a sampling frequency between 10 Hz and 500 Hz. The sample holder is fixed on a two-dimensional micrometer computer controlled translation stage. This allows to perform measurements of the velocity at 100 points on the surface of the sample, leading to the representation of the mode-shapes for each resonance.

To perform the electrical excitation, the two surfaces of the sample orthogonal to the \mathbf{x}_3 polarization axis are metalized. However, to generate a maximum number of modes, an electrode patterning has been used bringing to the front the modes' symmetry. One of the metalized face is then only partially covered by electrodes (Figure 3(b)) in a way to deliver enough electrical power while retaining a low electrical environment (null external field). In this configuration, the excitation of different points on the surface allows to select the desired modes. Figure 4(a) presents three selected excitation point on the surface of the cube. The corresponding measured electrical admittance of the PMN-34.5%PT ceramic cube reveals that the maximum excitation is obtained, for a vibration frequency of 87500 Hz, when the corner is excited while the two other excitations generate very low vibrations. This confirms the fact that the corresponding mode is mainly a torsion mode as shown in Table 2.

Because the sample is excited by the electrical analyzer and that mechanical velocities

are measured, the detected vibrations are necessary those of piezoactive modes meaning that full elastic, piezoelectric and dielectric tensors should be recoverable. As expected, a resonance of the real part of the electrical admittance, measured with the impedance analyzer, coincides with a mechanical resonance, measured with the laser probe (Figure 4(b)). Mechanical resonances are then first simply identified from the behavior of the real part of the electrical admittance.

4.2 Inverse problem and identification of the piezoelectric tensor

To identify the material characteristics, a fit procedure has been developed. It allows, modifying the C_{ijkl}^E , e_{ijk} and ε_{ij}^S tensors, to match the computed resonant frequencies to the measured data. Due to symmetry considerations, ten, respectively eleven, constants have to be identified for hexagonal ($6mm$) and tetragonal ($4mm$) symmetry materials, respectively. The identification protocol is performed on a PMN-34.5%PT ceramic and a PZN-12%PT single crystal. The sensitivity of each mode to the constants is first theoretically evaluated in a way to isolate the resonances mainly sensitive to only one particular characteristic. The mode sensitivity study presented in Table 5 is performed for the PMN-34.5%PT ceramic cube and can easily be transferred to the PZN-12%PT single crystal sample. Table 5 quantifies the resonant mode response in frequency resulting of a unity step applied on each constant independently. The most interesting modes, sensitive to one or two constants, are then revealed and the corresponding resonant frequencies are used to identify the corresponding characteristics. From Table 5, an order of the constant identification could be the following:

1. Mode A_g (2) : C_{12}^E ,
2. Mode B_{1g} (4) : C_{44}^E ,
3. Mode B_{1g} (2) : C_{66}^E ,
4. Mode $B_{2/3g}$ (2) : e_{15} ,
5. Mode A_u (3) : ε_{11}^S ,
6. Mode A_g (3) : $C_{11}^E, C_{33}^E, \varepsilon_{33}^S$
7. Mode $B_{2/3g}$ (8) : C_{13}^E, e_{31}, e_{33} .

In a second part, a global fit, based on the simplex routine [23], is performed on the remaining components of the electromechanical tensor.

4.3 Validation of the method on a PMN-34.5%PT cube

4.3.1 Direct problem

Figure 5 presents the measured modal displacements of the A_g mode and the corresponding computed ones for a $10.02 \times 10.02 \times 10.14$ mm³ cube of PMN-34.5%PT ceramic. At the surface of the cube, the displacements are of about 20 nm. Table 6 presents the comparison between the theoretical predictions and the measured frequencies for the corresponding identified modes in the range [85, 275] kHz. The experimental results are in accordance with the numerical simulations obtained from the initial tensors given in §3.1. The small differences can be explained by the fact that several shapes of samples were used to obtain these complete sets of characteristics and that our sample is not one of those of [21].

4.3.2 PMN-34.5PT characterization

To characterize our sample, the fitting procedure (§4.2) has been applied with the initial tensor given in [21]. Table 7 presents the identified characteristics after the fit procedure. The elastic, piezoelectric and dielectric constants identified from the sensitivity study have a precision less than 1% while those obtained from the global fit possess a tolerance from 2 to 3%. These tolerances correspond to characteristic modifications leading to an unchanged distance Δ_{mc} between the experimental data and the computed vibrations given by:

$$\Delta_{mc} = \frac{\sum_i \left| f_{\text{measured}}^{(i)} - f_{\text{computed}}^{(i)} \right|}{\sum_i f_{\text{measured}}^{(i)}} . \quad (20)$$

Table 7 shows that the identified constants are in good agreement with the initial ones [21]. The maximum difference is obtained on the C_{44}^E elastic constant and is of about 13%.

4.4 PZN-12%PT single crystal characterization

The resonant ultrasound spectroscopy method is now applied to the characterization of a $7.55 \times 7.52 \times 7.71 \text{ mm}^3$ PZN-12%PT single crystal cube (tetragonal phase). Our sample is polarized along the $[001]_c$ direction leading to a $4mm$ symmetry. The tested sample presents internal defects that might alter its resonant behavior (figure 6). However, the number of the measured modes and their corresponding resonant frequencies are supposed to be sufficient to identify the electromechanical characteristics of the cube.

No existing electromechanical tensor of a PZN-12%PT single crystal is available in the literature. However, some materials can possess very close properties especially a PMN-

$x\%$ PT single crystal with a PT ratio inducing a tetragonal symmetry. As a consequence, the electromechanical properties of a PMN-42%PT single crystal [24] were used to identify the resonant modes from their respective mode-shapes and the corresponding symmetry group defined in §2.2. Note that, while the PMN-42%PT single crystal vibrations possess the same resonant mode-shapes, the corresponding frequencies are different than those of the PZN-12%PT single crystal.

The studied PZN-12%PT single crystal cube has been prepared in a same way than the PMN-34.5%PT ceramic sample. In particular, a similar electrode patterning has been performed. Figure 6 presents the spectrum of the surface velocity measured on one of the upper corners, in a [94.5, 210] kHz frequency range. The measured resonant frequencies are presented in Table 8. The measured surface displacements are of about 15 nm. The A_g mode-shape measured on the PZN-12%PT cube at 122918 Hz is presented on figure 7. It is compared to the numerical one identified from the PMN-42%PT single crystal properties. As above, the characterization procedure (§4.2) has been applied to perform a fit of the computed frequencies to the measured ones. The characteristics presented in Table 9 report, to the authors knowledge, the first complete elastic, piezoelectric and dielectric tensors of a PZN-12%PT single crystal given in the literature. They are consistent with tensors of single crystals with close compositions [1, 2, 25].

5 Conclusion

This paper presents the characterization of a PMN-34.5%PT ceramic with the hexagonal symmetry ($6mm$) and a PZN-12%PT single crystal in the tetragonal phase ($4mm$). Res-

onant Ultrasound Spectroscopy measurements were performed on an experimental set-up where the electrical excitation of the sample and the laser detection of its mechanical displacements allow to study piezoelectric coupled vibration modes. Furthermore, a specific design of the sample electrodes has been proposed in a way to generate all mode symmetries. To solve the inverse problem and identify the material characteristics, an attention was particularly payed on the modes' sensitivity to independant elastic, piezoelectric or dielectric constants. The method is first validated on the characterization of a PMN-34.5%PT ceramic cube and results are found to be in good agreement with literature. The full tensor of a PZN-12%PT single crystal is then presented. The tested samples were of several hundreds of mm^3 but the instrumentation, and particularly the laser interferometer, should allow to identify characteristics of smaller materials. This may be very promissing for high frequency applications where few mm^3 materials are used leading to a high dependence of the device behavior to the material microstructure.

A Interaction matrices for a one side metalized parallelepiped

The descriptions of the matrices $\mathbf{\Gamma}$, $\mathbf{\Lambda}$ et $\mathbf{\Omega}$ are given in tables 10, 11 and 12. The functions describing the mechanical displacement are the same than in the non metalized case (9). The elastic interaction matrix is then that defined in [13]. Taking into account the functions φ_r ($r = 1, \dots, M$) of equation (18), the G_k ($k = 1, 2, \dots, 9$) constitutive of

the piezoelectric interaction matrix become:

$$\begin{aligned}
G_1 &= D_{\lambda\xi} \delta_{\mu\varsigma} C_{\nu\eta}^{(p)} / L_1^2, & G_2 &= \delta_{\lambda\xi} D_{\mu\varsigma} C_{\nu\eta}^{(p)} / L_2^2, \\
G_3 &= \delta_{\lambda\xi} \delta_{\mu\varsigma} D_{\nu\eta}^{(p)} / L_3^2, & G_4 &= \delta_{\lambda\xi} E_{\mu\varsigma} F_{\nu\eta}^{(p)} / L_2 L_3, \\
G_5 &= \delta_{\lambda\xi} F_{\mu\varsigma} E_{\nu\eta}^{(p)} / L_2 L_3, & G_6 &= F_{\lambda\xi} \delta_{\mu\varsigma} E_{\nu\eta}^{(p)} / L_3 L_1, \\
G_7 &= E_{\lambda\xi} \delta_{\mu\varsigma} F_{\nu\eta}^{(p)} / L_3 L_1, & G_8 &= E_{\lambda\xi} F_{\mu\varsigma} C_{\nu\eta}^{(p)} / L_1 L_2, \\
G_9 &= F_{\lambda\xi} E_{\mu\varsigma} C_{\nu\eta}^{(p)} / L_1 L_2,
\end{aligned} \tag{21}$$

with,

$$\begin{aligned}
C_{\nu\eta}^{(p)} &= \int_{-1}^1 \bar{P}_\nu(X) f_\eta(X) dX \\
&= \frac{1}{2\Pi} \begin{cases} 1 & \text{if } \nu = \eta, \\ (\nu + 1)/(2\nu + 3) & \text{if } \nu + 1 = \eta, \\ \nu/(2\nu - 1) & \text{if } \nu - 1 = \eta, \\ 0 & \text{else,} \end{cases}
\end{aligned} \tag{22}$$

$$\begin{aligned}
D_{\nu\eta}^{(p)} &= \int_{-1}^1 \frac{d\bar{P}_\nu(X)}{dX} \frac{df_\eta(X)}{dX} dX \\
&= \Pi \begin{cases} (\nu + 1)\nu/2 & \text{if } \nu < \eta, \\ (\eta + 1)\eta/2 & \text{if } \nu > \eta \text{ and } \nu + \eta \text{ even,} \\ ((\eta + 1)\eta + 2)/2 & \text{if } \nu > \eta \text{ and } \nu + \eta \text{ odd,} \end{cases}
\end{aligned} \tag{23}$$

$$\begin{aligned}
E_{\nu\eta}^{(p)} &= \int_{-1}^1 \bar{P}_\nu(X) \frac{df_\eta(X)}{dX} dX \\
&= \Pi \begin{cases} (\nu + 1)/(2\nu + 1) & \text{if } \nu = \eta, \\ 1 & \text{if } \nu < \eta, \\ 0 & \text{else,} \end{cases} \tag{24}
\end{aligned}$$

$$\begin{aligned}
F_{\nu\eta}^{(p)} &= \int_{-1}^1 \frac{d\bar{P}_\nu(X)}{dX} f_\eta(X) dX \\
&= \Pi \begin{cases} \nu/(2\nu + 1) & \text{if } \nu = \eta, \\ 1 & \text{if } \nu > \eta, \\ 0 & \text{else,} \end{cases} \tag{25}
\end{aligned}$$

where $\Pi = (-1)^\eta \sqrt{\frac{2\nu+1}{2}}$.

The G_k ($k = 1, 2, \dots, 9$) constitutive of the dielectric interaction matrix $\mathbf{\Lambda}$ (Table 12) become, for a one side metalized parallelepiped:

$$\begin{aligned}
G_1 &= D_{\xi\xi'} \delta_{\zeta\zeta'} C_{\eta\eta'}^{(d)} / L_1^2, & G_2 &= \delta_{\xi\xi'} D_{\zeta\zeta'} C_{\eta\eta'}^{(d)} / L_2^2, \\
G_3 &= \delta_{\xi\xi'} \delta_{\zeta\zeta'} D_{\eta\eta'}^{(d)} / L_3^2, & G_4 &= \delta_{\xi\xi'} E_{\zeta\zeta'} F_{\eta\eta'}^{(d)} / L_2 L_3, \\
G_5 &= \delta_{\xi\xi'} F_{\zeta\zeta'} E_{\eta\eta'}^{(d)} / L_2 L_3, & G_6 &= F_{\xi\xi'} \delta_{\zeta\zeta'} E_{\eta\eta'}^{(d)} / L_3 L_1, \\
G_7 &= E_{\xi\xi'} \delta_{\zeta\zeta'} F_{\eta\eta'}^{(d)} / L_3 L_1, & G_8 &= E_{\xi\xi'} F_{\zeta\zeta'} C_{\eta\eta'}^{(p)} / L_1 L_2, \\
G_9 &= F_{\xi\xi'} E_{\zeta\zeta'} C_{\eta\eta'}^{(p)} / L_1 L_2,
\end{aligned} \tag{26}$$

with,

$$\begin{aligned}
C_{\nu\eta}^{(d)} &= \int_{-1}^1 f_{\eta}(X) f_{\eta'}(X) dX \\
&= \Theta \begin{cases} (3\eta(\eta+1) - 2)/(4\eta(\eta+1) - 3) & \text{if } \eta = \eta', \\ \eta'/(2\eta' + 1) & \text{if } \eta + 1 = \eta', \\ \eta'/(2\eta' + 1) - 1 & \text{if } \eta - 1 = \eta', \\ \eta(\eta + \eta')/H & \text{if } \eta - 2 = \eta', \\ \eta'(\eta + \eta')/H & \text{if } \eta + 2 = \eta', \\ 0 & \text{else,} \end{cases} \quad (27)
\end{aligned}$$

$$(28)$$

where $\Theta = \frac{(-1)^{\eta+\eta'}}{2\eta+1}$, and $h = 4(2\eta' + 1)(\eta + \eta' + 1)$,

$$\begin{aligned}
D_{\eta\eta'}^{(d)} &= \int_{-1}^1 \frac{df_{\eta}(X)}{dX} \frac{df_{\eta'}(X)}{dX} dX \\
&= \begin{cases} (1 + 2\eta(\eta(\eta+1) + 1))/2(2\eta+1) & \text{if } \eta = \eta', \\ (-1)^{\eta+\eta'}(\eta(\eta+1) + 1)/2 & \text{if } \eta < \eta', \\ (-1)^{\eta+\eta'}(\eta'(\eta'+1) + 1)/2 & \text{if } \eta > \eta', \end{cases} \quad (29)
\end{aligned}$$

$$\begin{aligned}
E_{\eta\eta'}^{(d)} &= \int_{-1}^1 f_{\eta}(X) \frac{df_{\eta'}(X)}{dX} dX \\
&= (-1)^{\eta+\eta'} \begin{cases} 1/2 & \text{si } \eta = \eta', \\ \eta'^2/2(1 - 4\eta'^2) + 1 & \text{if } \eta + 1 = \eta', \\ \eta^2/2(1 - 4\eta^2) & \text{if } \eta - 1 = \eta', \\ 0 & \text{else,} \end{cases} \quad (30)
\end{aligned}$$

$$\begin{aligned}
F_{\eta\eta'}^{(d)} &= \int_{-1}^1 \frac{df_{\eta}(X)}{dX} f_{\eta'}(X) dX \\
&= (-1)^{\eta+\eta'} \begin{cases} 1/2 & \text{if } \eta = \eta', \\ \eta^2/2(1 - 4\eta^2) + 1 & \text{if } \eta - 1 = \eta', \\ \eta'^2/2(1 - 4\eta'^2) & \text{if } \eta + 1 = \eta', \\ 0 & \text{else.} \end{cases} \quad (31)
\end{aligned}$$

Similarly, $D_{\lambda\xi}$, $E_{\lambda\xi}$ et $F_{\lambda\xi}$ are given in [13].

Acknowledgment

This work was supported by the French Ministry of Research through the DEMonstrateur de nouveaux CRistaux piézoélectriques pour l'Imagerie et les Traitements Externes (DEMOCRITE) Réseau National des Technologies pour la Santé (RNTS) project, n ° CT03 B 439.

References

- [1] J. Kuwata, K. Uchino, and S. Nomura. Presynthesis of raw materials used for the growth of $\text{Pb}[(\text{Zn}_{1/3}\text{Nb}_{2/3})_{0.91}\text{Ti}_{0.09}]\text{O}_3$ single crystal by a modified Bridgman method. *Material Letters*, 52:423–428, 1982.
- [2] S.-E. Park and T. R. Shrout. Characteristics of Relaxor-Based Piezoelectric Single Crystals for Ultrasonic Transducers. *IEEE Transactions on Ultrasonics, Ferroelectrics, and Frequency control*, 44:1140–1146, 1997.
- [3] Bijun Fang, Haiqing Xu, Yongjun Wu, Haosu Luo, and Zhiwen Yin. Presynthesis of raw materials used for the growth of $\text{Pb}[(\text{Zn}_{1/3}\text{Nb}_{2/3})_{0.91}\text{Ti}_{0.09}]\text{O}_3$ single crystal by a modified Bridgman method. *Material Letters*, 52:423–428, 2002.
- [4] L. C. Lim and K. K. Rajan. High-homogeneity High-performance flux-grown $\text{Pb}(\text{Zn}_{1/3}\text{Nb}_{2/3})\text{O}_3$ -(6-7)% PbTiO_3 single crystals. *Journal of Crystal Growth*, 271:435–444, 2004.
- [5] Diouma Kobor. *Synthèse, dopage et caractérisation de monocristaux ferroélectrique type PZN-PT par la méthode du flux*. PhD thesis, Institut National des Sciences Appliquées de Lyon, dec. 2005.
- [6] IEEE. Publication and Proposed Revision of ANSI/IEEE Standard 176-1987 "ANSI/IEEE Standard on piezoelectricity". *IEEE Transaction on Ultrasonics, Ferroelectrics and Frequency Control*, 52:423–428, 2002.

- [7] Rui Zhang, Bei Jiang, Wenhua Jiang, and Wenwu Cao. Complete set of properties of $0.92\text{Pb}(\text{Zn}_{1/3}\text{Nb}_{2/3})\text{O}_3\text{-}0.08\text{PbTiO}_3$ single crystal with engineered domains. *Materials Letters*, 57:1305–1308, 2003.
- [8] Emmanuel Le Clézio and Alexander Shuvalov. Transmission of acoustic waves through piezoelectric plates: modeling and experiment. In *Proc. IEEE Ultrasonic Symposium*, pages 553–556, Montreal, Canada, août 2004.
- [9] E. Le Clézio, M. Lam, J. Fortineau, E. Ringgaard, R. Lou-Møller, and G. Feuillard. Tensor characterisation of high permittivity pzt-nn materials for ultrasonic applications. Liberec Czech Republic, February 7-9 2007.
- [10] R.G. Leisure and F.A. Willis. Resonant ultrasound spectroscopy. *Journal of Physics : Condensed Matter*, 9:6001–6029, 1997.
- [11] Lev Ostrovsky, Andrey Lebdev, Alexander Matveyev, Andrey Potapov, Alexander Sutin, Irina Soustova, and Paul Johnson. Application of three-dimensional resonant acoustic spectroscopy method to rock and building materials. *Journal of the Acoustical Society of America*, 110(4):1770–1777, 2001.
- [12] Jiri Plesek, Radek Kolman, and Michal Landa. Using finite element method for the determination of elastic moduli by resonant ultrasound spectroscopy. *Journal of the Acoustical Society of America*, 116(1):282–287, 2004.
- [13] Ichiro Ohno. Rectangular Parallelepiped Resonance Method for Piezoelectric Crystals and Elastic Constants of Alpha-Quartz. *Physics and Chemistry of Minerals*, 17:371–378, 1990.

- [14] Hirotsugu Ogi, Yasunori Kawasaki, Masahiko Hirao, and Hassel Ledbetter. Acoustic Spectroscopy of Lithium Niobate: Elastic and Piezoelectric Coefficients. *Journal of Applied Physics*, 92(5):2451–2456, 2002.
- [15] E. P. E. Nisse. Variational method for electroelastic vibration analysis. *IEEE Transactions On Sonics And Ultrasonics*, 14:53–160, 1967.
- [16] Richard Holland. Resonant properties of piezoelectric ceramics rectangular parallelepiped. *The Journal of the Acoustical Society of America*, 43:988–997, 1967.
- [17] Ichiro Ohno. Free Vibration of a Rectangular Parallelepiped Crystal and Its Application to Determination of Elastic Constants of Orthorhombic Crystals. *Journal Physic on Earth*, 24:355–379, 1976.
- [18] William M. Visscher, Albert Migliori, Thomas M. Bell, and Robert A. Reinert. On the Normal Modes of Free Vibration of Homogeneous and Anisotropic Elastic Objects. *Journal of the Acoustical Society of America*, 90:2154–2161, 1991.
- [19] Eiji Mochizuki. Application of Group Theory to Free Oscilations of an Anisotropic Rectangular Parallelepiped. *Journal Physic on Earth*, 35:159–170, 1987.
- [20] C. J. H. Schutte, J. E. Bertie, P. R. Bunker, J. T. Hougen, I. M. Mills, J. K. G. Watson, and B. P. Winnewisser. Notations and conventions in molecular spectroscopy : Part 2. Symmetry notation. *Pure and Applied Chemistry*, 69:1641–1649, 1997.
- [21] Henri Hemery. *Céramiques orientées hautes performances : $Pb(Mg_{1/3}Nb_{2/3})O_3$ - $PbTiO_3$ par croissance interfaciale*. PhD thesis, Ecole Centrale de Paris, dec. 2003.

- [22] A. Migliori, J. L. Sarrao, William M. Visscher, T. M. Bell, Ming Lei, Z. Fisk, and R.G. Leisure. Resonant Ultrasound Spectroscopic Technics for Measurement of the Elastic Moduli of Solids. *Physica B*, 183:1–24, 1993.
- [23] J. A. Nelder and R. Mead. A simplex method for function minimization. *Computer Journal*, 7:308–313, 1965.
- [24] Hu Cao, V. Hugo Schimidt, Rui Zhang, Wenwu Cao, and Haosu Luo. Elastic, piezoelectric, and dielectric properties of $0.58\text{Pb}(\text{Mg}_{1/3}\text{Nb}_{2/3})\text{O}_3\text{-}0.42\text{PbTiO}_3$ single crystal. *Journal of Applied Physics*, 96(1):549–554, 2004.
- [25] A. Dabkowski, H. A. Dabkowska, J.E. Greedan, W. Ren, and B. K. Mukherjee. Growth and properties of single crystals of relaxor pzn-pt materials obtained from high-temperature solution. *Journal of Crystal Growth*, 265:204–213, 2004.
- [26] Jr Harold H. Demarest. Cube-Resonance Method to Determine the Elastic Constants of Solids. *The Journal of the Acoustical Society of America*, 49(3):768–775, 1971.
- [27] Hassel Ledbetter, Hirotsugu Ogi, and Nobutomo Nakamura. Elastic, Anelastic, Piezoelectric Coefficients of Monocrystal Lithium Niobate. *Mechanics of Materials*, 36:941–947, 2003.

LIST OF TABLES

Table 1. Normal mode classification for the orthorhombic symmetry class mmm . e and o correspond to even and odd respectively.

Table 2. Normal mode classification for a $10 \times 10 \times 10 \text{mm}^3$ PMN-34.5%PT ceramic.

Table 3. Resonant frequencies of a $10 \times 10 \times 10 \text{mm}^3$ PMN-34.5%PT doped Manganese cube (Hz).

Table 4. Comparison between the resonant frequencies of a non metalized and a metalized cube.

Table 5. PMN-34.5%PT ceramic cube mode sensitivity to a unity variation of one characteristic.

Table 6. Measured resonant frequencies in the range 85 kHz - 275 kHz for a PMN-34.5%PT ceramic cube.

Table 7. PMN-34.5%PT ceramic cube properties identified by Resonant Ultrasound Spectroscopy.

Table 8. Measured resonances of the PZN-12%PT single crystal cube and corresponding identified modes.

Table 9. PZN-12%PT single crystal cube properties identified by acoustic spectroscopy.

Table 10. Elastic interaction matrix $\mathbf{\Gamma}$.

Table 11. Piezoelectric interaction matrix $\mathbf{\Omega}$.

Table 12. Dielectric interaction matrix $\mathbf{\Lambda}$.

LIST OF FIGURES

Fig. 1. Rectangular parallelepiped of characteristic lengths $L_1 = \frac{A}{2}$, $L_2 = \frac{B}{2}$, $L_3 = \frac{C}{2}$.

Fig. 2. Comparison between free resonance mode-shapes and electrical potentials computed, on the upper surface $x_3 = L_3$, from the variational method and the FE simulation code. Axis \mathbf{x}_1 and \mathbf{x}_2 are respectively horizontal and vertical. The resonant frequencies are respectively 114431 Hz (VM) and 114450 Hz (EF).

Fig. 3. Experimental set-up and tested sample.

Fig. 4. Excitation of piezoelectric coupled modes and electrode design revealing the mode symmetry for the PMN-34.5%PT ceramic cube.

Fig. 5. Experimental (a) and theoretical (b) vibration mode-shapes at the upper surface of the PMN-34.5%PT cube ($x_3 = L_3$).

Fig. 6. PZN-12%PT single crystal cube and the corresponding surface velocity spectrum measured on one of the upper corners for frequencies ranging from 94500 Hz to 210000 Hz.

Fig. 7. Computed and A_g measured vibration mode-shapes at one surface of the PZN-12%PT cube.

A_g		λ	μ	ν	A_u		λ	μ	ν
	$a_{\lambda\mu\nu 1}$	o	e	e		$a_{\lambda\mu\nu 1}$	e	o	o
	$a_{\lambda\mu\nu 2}$	e	o	e		$a_{\lambda\mu\nu 2}$	o	e	o
	$a_{\lambda\mu\nu 3}$	e	e	o		$a_{\lambda\mu\nu 3}$	o	o	e
		ξ	ς	η		ξ	ς	η	
	$b_{\lambda\mu\nu}$	e	e	o		$b_{\lambda\mu\nu}$	o	o	e
B_{1g}		λ	μ	ν	B_{1u}		λ	μ	ν
	$a_{\lambda\mu\nu 1}$	e	o	e		$a_{\lambda\mu\nu 1}$	o	e	o
	$a_{\lambda\mu\nu 2}$	o	e	e		$a_{\lambda\mu\nu 2}$	e	o	o
	$a_{\lambda\mu\nu 3}$	o	o	o		$a_{\lambda\mu\nu 3}$	e	e	e
		ξ	ς	η		ξ	ς	η	
	$b_{\lambda\mu\nu}$	o	o	o		$b_{\lambda\mu\nu}$	e	e	e
B_{2g}		λ	μ	ν	B_{2u}		λ	μ	ν
	$a_{\lambda\mu\nu 1}$	e	e	o		$a_{\lambda\mu\nu 1}$	o	o	e
	$a_{\lambda\mu\nu 2}$	o	o	o		$a_{\lambda\mu\nu 2}$	e	e	e
	$a_{\lambda\mu\nu 3}$	o	e	e		$a_{\lambda\mu\nu 3}$	e	o	o
		ξ	ς	η		ξ	ς	η	
	$b_{\lambda\mu\nu}$	o	e	e		$b_{\lambda\mu\nu}$	e	o	o
B_{3g}		λ	μ	ν	B_{3u}		λ	μ	ν
	$a_{\lambda\mu\nu 1}$	o	o	o		$a_{\lambda\mu\nu 1}$	e	e	e
	$a_{\lambda\mu\nu 2}$	e	e	o		$a_{\lambda\mu\nu 2}$	o	o	e
	$a_{\lambda\mu\nu 3}$	e	o	e		$a_{\lambda\mu\nu 3}$	o	e	o
		ξ	ς	η		ξ	ς	η	
	$b_{\lambda\mu\nu}$	e	o	e		$b_{\lambda\mu\nu}$	o	e	o

Table 1:

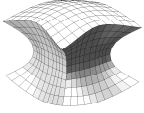
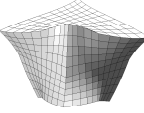
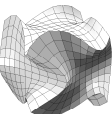
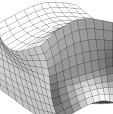
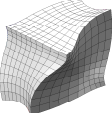
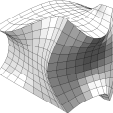
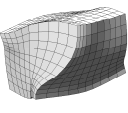
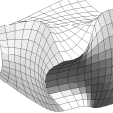
Mode	Resonant frequency	Mode shape	Mode	Resonant frequency	Mode shape
A_g	124892 Hz		A_u	86356 Hz	
	126963 Hz			88345 Hz	
	151755 Hz				
	166493 Hz				
B_{1g}	112133 Hz		B_{1u}	114431 Hz	
	139257 Hz			164086 Hz	
	167537 Hz			168691 Hz	
B_{2g}	133978 Hz		B_{2u}	111470 Hz	
	153178 Hz			139062 Hz	
	167337 Hz			167254 Hz	
B_{3g}	133978 Hz		B_{3u}	111470 Hz	
	153178 Hz			139062 Hz	
	167337 Hz			167254 Hz	

Table 2:

Variational model	86356	88345	111470	111470	112133	114431
FE model	86419	88384	112311	112311	112225	114450
Difference (%)	-0.07	-0.04	-0.75	-0.75	-0.08	-0.13
Variational model	124892	126963	133978	133978	139062	139062
FE model	125610	126961	134169	134169	139466	139466
Difference (%)	-0.57	0.001	-0.14	-0.14	-0.29	-0.29
Variational model	139257	151755	153178	153178	164086	166493
FE model	140412	153629	153213	153213	164572	166637
Difference (%)	-0.83	-1.23	-0.02	-0.02	-0.29	-0.09
Variational model	167254	167254	167337	167337	167537	168691
FE model	167646	167646	168073	168073	167807	169318
Difference (%)	-0.23	-0.23	-0.44	-0.44	-0.16	-0.37

Table 3:

Variationnal Method		F. E. Simulations	
$-L_3$ Face metalized	Difference with no electrode	$-L_3$ Face metalized	Difference with no electrode
85131 Hz	-1.42 %	85367 Hz	-1.22 %
88337 Hz	-0.01 %	88382 Hz	0.00 %
108148 Hz	-2.98 %	108780 Hz	-3.14 %
108148 Hz	-2.98 %	108780 Hz	-3.14 %
111850 Hz	-0.25 %	111938 Hz	-0.26 %
113955 Hz	-0.42 %	114403 Hz	-0.04 %
124141 Hz	-0.60 %	124313 Hz	-1.03 %
126963 Hz	0.00 %	126960 Hz	0.00 %
127631 Hz	-4.74 %	128239 Hz	-4.42 %
127631 Hz	-4.74 %	128239 Hz	-4.42 %
138745 Hz	-0.23 %	139107 Hz	-0.26 %
138745 Hz	-0.23 %	139107 Hz	-0.26 %
136826 Hz	-1.75 %	137334 Hz	-2.19 %
151206 Hz	-0.36 %	152726 Hz	-0.59 %
152899 Hz	-0.18 %	152646 Hz	-0.37 %
152899 Hz	-0.18 %	152646 Hz	-0.37 %
161225 Hz	-1.74 %	164059 Hz	-0.31 %
165260 Hz	-0.74 %	164902 Hz	-1.04 %
Maximum relative difference: -4.73%		Maximum relative difference: -4.42%	
Mean relative difference: 1.31%		Mean relative difference: 1.28%	

Table 4:

Mode	Hz / GPa						Hz / (C/m ²)			Hz / (nF/m)	
	C_{11}^E	C_{33}^E	C_{44}^E	C_{66}^E	C_{12}^E	C_{13}^E	e_{15}	e_{31}	e_{33}	ϵ_{11}^S	ϵ_{33}^S
A_g (2)	604	0	0	0	-1225	-14	0	-3	0	0	0
A_g (3)	233	596	3	7	236	-632	6	817	1436	-48	-1064
B_{1g} (2)	17	23	1	2004	-3	-28	-4	-14	24	-5	-7
B_{1g} (4)	126	90	1016	76	-180	-87	13	-14	31	-13	-5
$B_{2/3g}$ (2)	62	68	1278	3	-203	63	1045	43	58	-437	-16
$B_{2/3g}$ (8)	1061	878	289	211	-152	-1935	-293	-1757	1591	-381	-845
A_u (2)	9	2	738	512	-16	-2	44	0	0	0	0
A_u (3)	22	98	799	840	2	-67	727	-10	21	-289	-6

Table 5:

Measured f_r	Symmetry group	Computations	Measured f_r	Symmetry group	Computations
88750 Hz	A_u	86537 Hz	209100 Hz	B_{1u}	209709 Hz
107900 Hz	$B_{2u} - B_{3u}$	110236 Hz	212100 Hz	$B_{2g} - B_{3g}$	217815 Hz
119600 Hz	B_{1g}	111916 Hz	229800 Hz	A_g	230660 Hz
138700 Hz	B_{1g}	137661 Hz	241500 Hz	A_g	238011 Hz
148700 Hz	A_g	150606 Hz	249700 Hz	$B_{2u} - B_{3u}$	246100 Hz
168500 Hz	B_{1u}	164217 Hz	252900 Hz	B_{1u}	233247 Hz
178600 Hz	A_g	180455 Hz	258700 Hz	A_g	267737 Hz
206600 Hz	$B_{2u} - B_{3u}$	212839 Hz			

Table 6:

Properties		Unity	Values from [21]	Identified values
Density	ρ	kg/mm ³	8060	
Elastic constants	C_{11}^E	GPa	168,8	174,7
	C_{12}^E	GPa	116,83	116,61
	C_{13}^E	GPa	116,80	119,3
	C_{33}^E	GPa	154,43	154,8
	C_{44}^E	GPa	30,56	26,7
	C_{66}^E	GPa	25,97	29,0
Dielectric permittivity	ε_{11}^S	ε_0	2367	2373
	ε_{33}^S	ε_0	2622	2825
Piezoelectric constants	e_{15}	C/m ²	16,66	17,1
	e_{31}	C/m ²	-6,92	-6,4
	e_{33}	C/m ²	30,15	27,3
Δ_{mc}			$5,2 \cdot 10^{-2}$	$1,8 \cdot 10^{-2}$

Table 7:

Measurements	Symmetry group	Measurements	Symmetry group
82750 Hz	$B_{2u} - B_{3u}$	396871 Hz	A_g
108495 Hz	A_g	314504 Hz	A_g
122918 Hz	A_g	293695 Hz	A_g
136818 Hz	A_u	288500 Hz	A_u
161336 Hz	A_g	251734 Hz	$B_{2u} - B_{3u}$
168527 Hz	B_{1u}	203693 Hz	$B_{2g} - B_{3g}$
191593 Hz	$B_{2u} - B_{3u}$	195184 Hz	A_u

Table 8:

Properties		Unity	Values	Tolerance
Density	ρ	kg/mm ³	8380	
Elastic constants	C_{11}^E	GPa	152	± 2
	C_{12}^E	GPa	87	± 1
	C_{13}^E	GPa	90	$\pm 0,5$
	C_{33}^E	GPa	84	± 2
	C_{44}^E	GPa	37	± 3
	C_{66}^E	GPa	22	± 1
Dielectric permittivity	ε_{11}^S	ε_0	2420	± 150
	ε_{33}^S	ε_0	331	± 50
Piezoelectric constants	e_{15}	C/m ²	35	± 3
	e_{31}	C/m ²	-3	$\pm 0,5$
	e_{33}	C/m ²	4	± 1
Δ_{mc}			0,95	

Table 9:

(i,j)	$\Gamma_{pp'}$
(1,1)	$C_{11}^E G_1 + C_{66}^E G_2 + C_{55}^E G_3 + C_{56}^E G_4 + C_{56}^E G_5 + C_{15}^E G_6 + C_{15}^E G_7 + C_{16}^E G_8 + C_{16}^E G_9$
(2,2)	$C_{66}^E G_1 + C_{22}^E G_2 + C_{44}^E G_3 + C_{24}^E G_4 + C_{24}^E G_5 + C_{46}^E G_6 + C_{46}^E G_7 + C_{26}^E G_8 + C_{26}^E G_9$
(3,3)	$C_{55}^E G_1 + C_{44}^E G_2 + C_{33}^E G_3 + C_{14}^E G_4 + C_{14}^E G_5 + C_{35}^E G_6 + C_{35}^E G_7 + C_{36}^E G_8 + C_{36}^E G_9$
(2,3)	$C_{56}^E G_1 + C_{24}^E G_2 + C_{34}^E G_3 + C_{44}^E G_4 + C_{23}^E G_5 + C_{36}^E G_6 + C_{45}^E G_7 + C_{25}^E G_8 + C_{46}^E G_9$
(3,1)	$C_{15}^E G_1 + C_{46}^E G_2 + C_{35}^E G_3 + C_{36}^E G_4 + C_{45}^E G_5 + C_{55}^E G_6 + C_{13}^E G_7 + C_{14}^E G_8 + C_{56}^E G_9$
(1,2)	$C_{16}^E G_1 + C_{26}^E G_2 + C_{45}^E G_3 + C_{25}^E G_4 + C_{46}^E G_5 + C_{14}^E G_6 + C_{56}^E G_7 + C_{66}^E G_8 + C_{12}^E G_9$

Table 10:

i	Ω_{pr}
1	$e_{11}G_1 + e_{26}G_2 + e_{35}G_3 + e_{25}G_4 + e_{36}G_5 + e_{31}G_6 + e_{15}G_7 + e_{16}G_8 + e_{21}G_9$
2	$e_{16}G_1 + e_{22}G_2 + e_{34}G_3 + e_{24}G_4 + e_{32}G_5 + e_{36}G_6 + e_{14}G_7 + e_{12}G_8 + e_{26}G_9$
3	$e_{15}G_1 + e_{24}G_2 + e_{33}G_3 + e_{23}G_4 + e_{34}G_5 + e_{35}G_6 + e_{13}G_7 + e_{14}G_8 + e_{25}G_9$

Table 11:

$\Lambda_{rr'}$
$\varepsilon_{11}^S G_1 + \varepsilon_{22}^S G_2 + \varepsilon_{33}^S G_3 + \varepsilon_{23}^S G_4 + \varepsilon_{32}^S G_5 + \varepsilon_{13}^S G_6 + \varepsilon_{31}^S G_7 + \varepsilon_{12}^S G_8 + \varepsilon_{21}^S G_9$

Table 12:

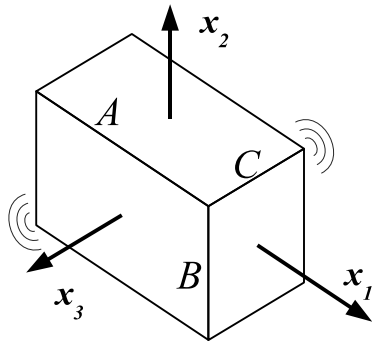
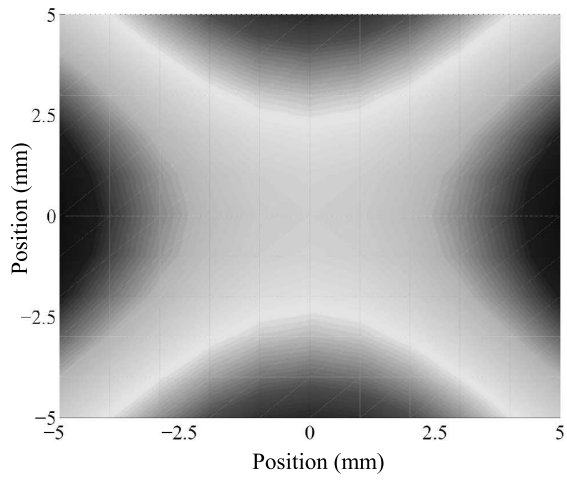
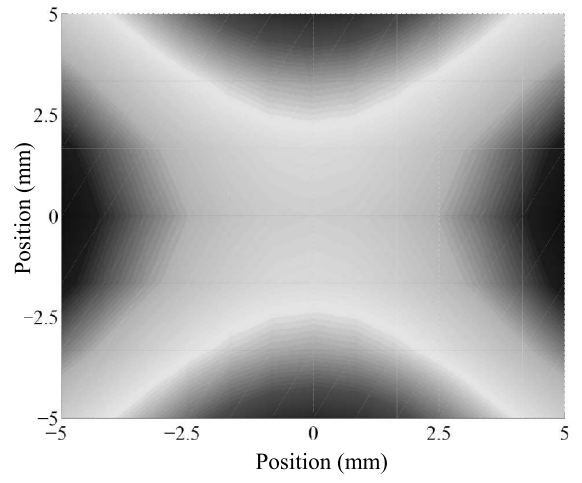


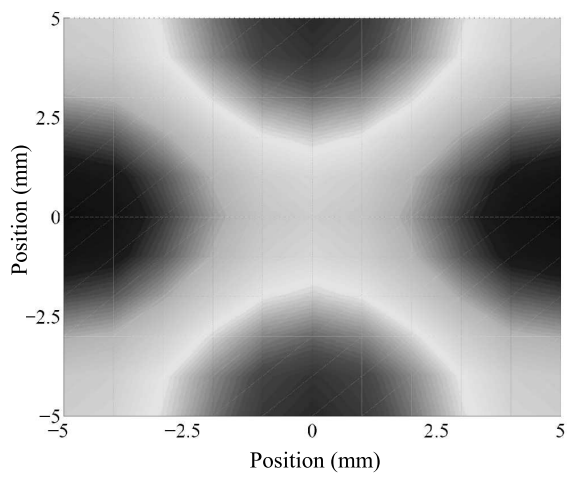
Figure 1:



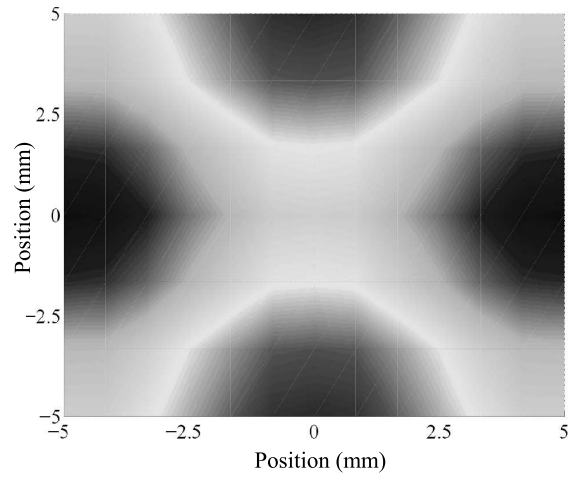
(a)



(b)

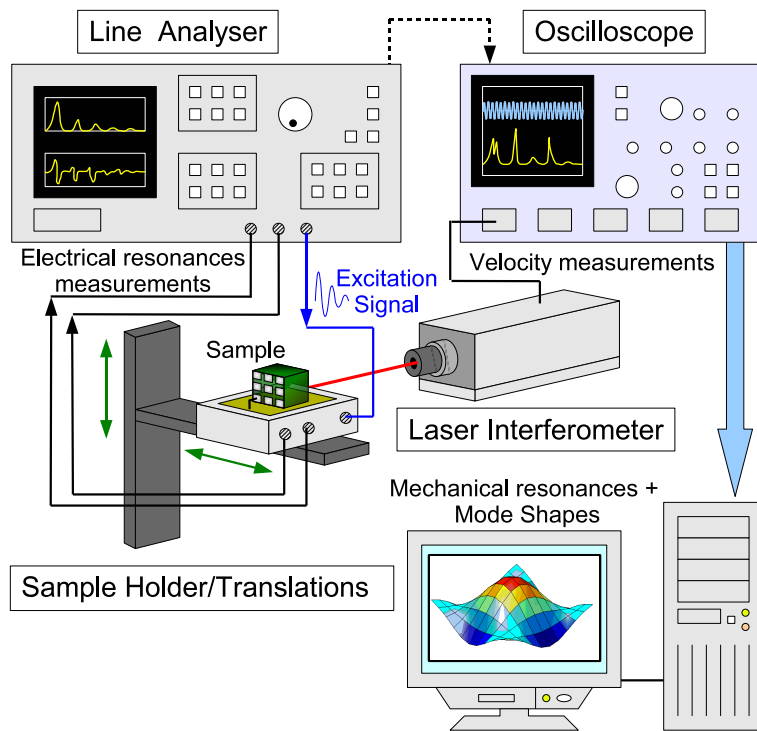


(c)

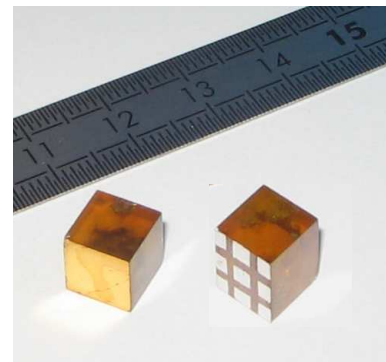


(d)

Figure 2:

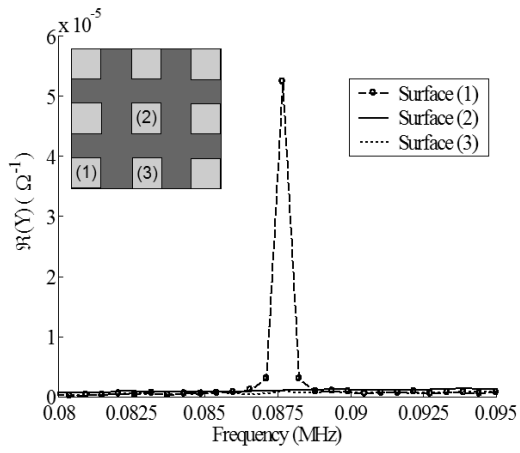


(a) Experimental set-up

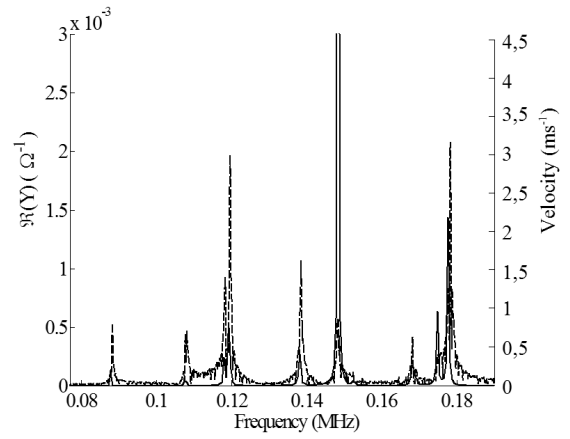


(b) Cube with designed electrode

Figure 3:

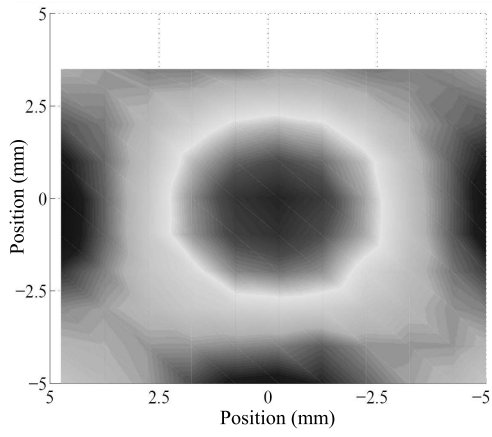


(a) real part of the electrical admittance for three different excitation points.



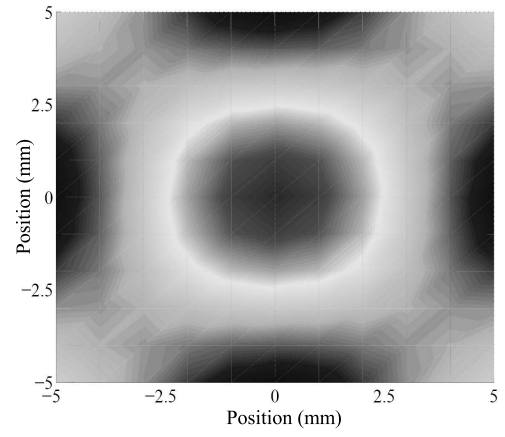
(b) Superposition of the electrical and mechanical resonance spectra of the PMN-34.5%PT ceramic cube.

Figure 4:



(a) Measured at 241500 Hz

A_g



(b) Computed at 238011 Hz

Figure 5:

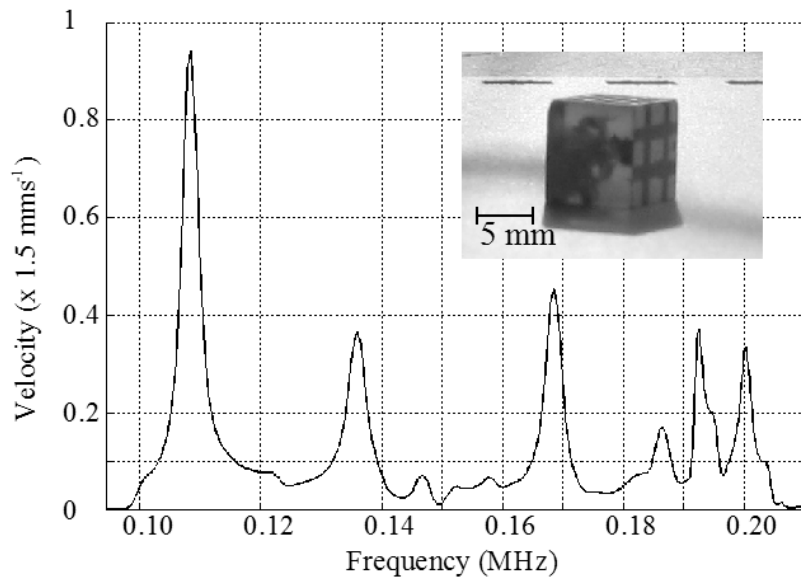


Figure 6:

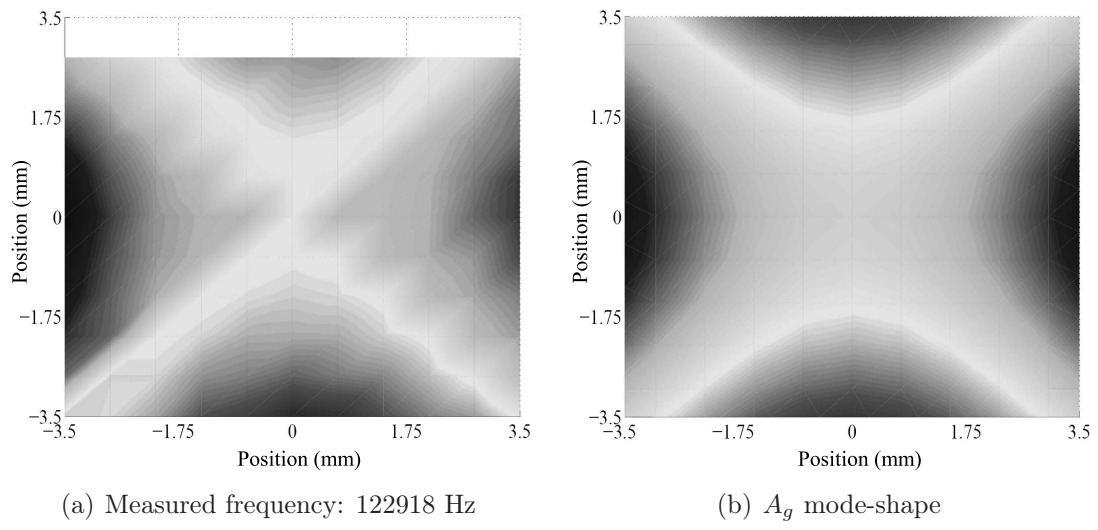


Figure 7: